Monthly Notices
of the
ROYAL ASTRONOMICAL SOCIETY
MNRAS **446,** 1641–1656 (2015) doi:10.1093/mnras/stu2170

Stellar models of multiple populations in globular clusters – I. The main sequence of NGC 6752

Aaron Dotter,[1★] Jason W. Ferguson,[2] Charlie Conroy,[3] A. P. Milone,[1] A. F. Marino[1] and David Yong[1]

[1] *Research School of Astronomy and Astrophysics, Australian National University, Canberra, ACT, 2611, Australia*
[2] *Department of Mathematics, Statistics, and Physics, Wichita State University, Wichita, 67260, KS, USA*
[3] *Department of Astronomy and Astrophysics, University of California, 95064, Santa Cruz, CA, USA*

Accepted 2014 October 16. Received 2014 October 15; in original form 2014 August 14

ABSTRACT

We present stellar atmosphere and evolution models of main-sequence stars in two stellar populations of the Galactic globular cluster NGC 6752. These populations represent the two extremes of light-element abundance variations in the cluster. NGC 6752 is a benchmark cluster in the study of multiple stellar populations because of the rich array of spectroscopic abundances and panchromatic *Hubble Space Telescope* photometry. The spectroscopic abundances are used to compute stellar atmosphere and evolution models. The synthetic spectra for the two populations show significant differences in the ultraviolet and, for the coolest temperatures, in the near-infrared. The stellar evolution models exhibit insignificant differences in the Hertzsprung-Russell (H–R) diagram except on the lower main sequence. The appearance of multiple sequences in the colour–magnitude diagrams (CMDs) of NGC 6752 is almost exclusively due to spectral effects caused by the abundance variations. The models reproduce the observed splitting and/or broadening of sequences in a range of CMDs. The ultraviolet CMDs are sensitive to variations in carbon, nitrogen, and oxygen but the models are not reliable enough to directly estimate abundance variations from photometry. On the other hand, the widening of the lower main sequence in the near-infrared CMD, driven by oxygen variation via the water molecule, is well described by the models and can be used to estimate the range of oxygen present in a cluster from photometry. We confirm that it is possible to use multiband photometry to estimate helium variations among the different populations, with the caveat that the estimated amount of helium enhancement is model dependent.

Key words: stars: abundances – stars: evolution – globular clusters: individual: NGC 6752.

1 INTRODUCTION

The study of chemical abundance variations in globular clusters (GCs) has a long history, the essence of which is captured in reviews by Freeman & Norris (1981), Gratton, Sneden & Carretta (2004), and Gratton, Carretta & Bragaglia (2012). Recent work has vastly increased the number of GCs in which such variations are observed as well as the sample size in a given cluster (e.g. Marino et al. 2008, 2011; Yong et al. 2008; Carretta et al. 2009a,b, and so on). These studies highlight the spread in light elements, especially the well-established anticorrelations between oxygen and sodium and, to a lesser extent, magnesium and aluminium. These variations are connected with the products of nuclear burning at temperatures appropriate for the hot CNO cycle (e.g. Prantzos, Charbonnel & Iliadis 2007), in intermediate- and high-mass stars, though the exact source of the nucleosynthesis site and nature of the pollution mechanism remain the subject of debate.

Identifying distinct sequences within a single GC solely from photometry began with the red giant branch (RGB; Lee et al. 1999) and main sequence (MS; Anderson 1997; Bedin et al. 2004) of ω Centauri. Photometric discovery of multiple sequences has accelerated with the sensitivity and resolution of detectors on board the *Hubble Space Telescope* (*HST*); see Piotto (2009) for a review of discoveries up until that time. The ultraviolet-visual (UVIS) and infrared (IR) channels of the *HST* Wide Field Camera 3 (WFC3) are the most effective means of detecting multiple photometric sequences available at present (e.g. Milone et al. 2013).

The link between multiple stellar sequences in the colour–magnitude diagram (CMD), as observed photometrically, and light-element abundance variations, as observed spectroscopically, is an area of active research. Meanwhile, there have been a handful of studies that model the appearance of multiple stellar populations

★ E-mail: aaron.dotter@gmail.com

Published by Oxford University Press on behalf of the Royal Astronomical Society

Table 1. Average abundance ratios from spectroscopy.

Ratio	Population A	C
[Fe/H]	−1.65	−1.61
[C/Fe]	−0.25	−0.70
[N/Fe]	−0.11	+1.35
[O/Fe]	+0.65	+0.03
[Na/Fe]	−0.03	+0.61
[Mg/Fe]	+0.51	+0.40
[Al/Fe]	+0.28	+1.14
[Si/Fe]	+0.27	+0.35
[S/Fe]	+0.25	+0.25
[Ca/Fe]	+0.21	+0.27
[Ti/Fe]	+0.10	+0.15
[V/Fe]	−0.34	−0.25
[Mn/Fe]	−0.50	−0.45
[Co/Fe]	−0.03	−0.06
[Ni/Fe]	−0.06	−0.03
[Cu/Fe]	−0.66	−0.60

in GCs. The first major work on the influence of light-element abundance variations on stellar evolution models is that of Salaris et al. (2006), who compared stellar evolution models with a typical α-enhanced abundance pattern (oxygen-rich) to models with a composition reflective of the extreme end of the observed abundance variations (oxygen-poor). Salaris et al. found that the abundance variations produce quite a small spread in effective temperature ($T_{\rm eff}$) for coeval populations and, therefore, CMDs comprising broad-band, optical filters could only show large spreads in the presence of a significant variation in helium. Pietrinferni et al. (2009) expanded the BaSTI data base of stellar evolution models to include light-element variations following the same abundance pattern as Salaris et al. (2006), with masses from 0.4 to 1.2 $M_{\odot}$.

Sbordone et al. (2011) made the first systematic comparison of model atmospheres and synthetic spectra from 3000 to 10 000Å computed with the abundance patterns of Salaris et al. (2006). Models were computed for [Fe/H] = −1.62 at eight different $T_{\rm eff}$–log (g) pairs corresponding to MS, subgiant, and red giant stars in the BaSTI isochrones. The authors found modest differences in the atmosphere structures due to variations in the light elements. On the other hand, the synthetic spectra and associated colour transformations were significantly influenced by differences in the absorption of carbon-, nitrogen-, and oxygen-bearing molecules at wavelengths shorter than 4000 Å, while leaving longer wavelengths essentially unchanged; the near-infrared (near-IR) was not considered.

Sbordone et al. recommend broad-band U and B filters, as well as Strömgren u, v, and y, to maximize the separation of GC stars in the CMD. The authors found that increasing the helium content made essentially no change to the model atmospheres and synthetic spectra and, thus, its influence is restricted to the interior models (in agreement with Girardi et al. 2007). Sbordone et al. (2011) found the separation of the sequences in a variety of CMDs to be consistent with observations but made no direct comparison between their models and photometry.

di Criscienzo, D'Antona & Ventura (2010) used the *HST* photometry of NGC 6397 (Richer et al. 2008) and predictions for the enhancement of helium, carbon, nitrogen, and oxygen at the metallicity of the cluster to estimate the allowed spread in helium of 2 per cent by mass (ΔY = 0.02) assuming that C+N+O remains roughly constant or as much as 4 per cent ($\Delta Y = 0.04$) if C+N+O is allowed to increase along with helium. The photometry used in this case was limited to the $F606W$ and $F814W$ bands that are insensitive to abundance variations (see Sbordone et al. 2011, and Sections 3 and 4 of this paper).

This paper presents a case study of the Galactic GC NGC 6752 that, due to its proximity and other distinguishing characteristics, has been the focus of significant observational effort in both spectroscopy (Grundahl et al. 2002; Yong et al. 2003, 2005, 2008, 2013) and photometry (Milone et al. 2010, 2013). These complimentary data sets invite a careful, data-driven study of NGC 6752.

The collective works of Yong, Grundahl, and collaborators on NGC 6752 are particularly useful in the sense that their data set includes sufficient information to piece together more or less the full picture of light-element variations for more than 20 red giants. Furthermore, the abundance of nitrogen is derived not from CN, but from NH, whose measurement is independent of the carbon abundance. Sufficient information is present in this data set to accurately model, in detail, the stars in NGC 6752 with very little in the way of assumptions regarding the abundances that are significant for stellar evolution models (Dotter et al. 2007b; VandenBerg et al. 2012) as well as for synthetic spectra and the associated bolometric corrections that are necessary to compare stellar evolution models to photometry.

The *HST* photometry presented by Milone et al. (2013) comprises data reaching down the MS in 15 filters from $F225W$ in the ultraviolet (UV) to $F160W$ in the near-IR; see their table 1 for details. The multiple sequences revealed in these data exhibit a complex range of behaviours. Based on these observations, Milone et al. have identified three stellar populations (labelled A, B, and C) that can be traced through different evolutionary phases in the CMDs. The RGB stars in these populations can also be matched with the spectroscopic targets of Yong et al.; this allows average abundances to be estimated for each population (table 2 of Milone et al. 2013).

The goal of the paper is to use the available abundance measurements to compute self-consistent stellar atmosphere and evolution models of stars at either end of the range of abundance variations (that is, for populations A and C) and then compare the *HST* photometry with those models along the MS. The stellar atmospheres and synthetic spectra are computed with two independent codes. If the models are successful in tracing the observed sequences, then they constitute a powerful tool for interpreting the observed behaviour in terms of the physical conditions found along the MS of NGC 6752 and, by extension, other GCs for which observations of comparable quantity may be obtained.

The remainder of the paper is organized as follows. Section 2 lays out the abundances that will be used to construct models; full details are included as an appendix. Section 3 describes the stellar atmosphere and spectrum synthesis codes and the models made by them. Section 4 describes the stellar evolution models and isochrones. Section 5 presents detailed comparisons of the transformed isochrones with the *HST* photometry. Section 6 summarizes the important results and discusses future directions for this work.

2 ELEMENTAL ABUNDANCES IN NGC 6752

We have adopted the collection of abundances reported by Yong et al. (2003, 2005, 2008). In particular, we refer to the photometric identification of stellar populations A and C by Milone et al. (2013) and their average abundances summarized in table 2 of that paper. While Milone et al. (2013) have also identified an intermediate population (B), we have chosen not to include it in this study because

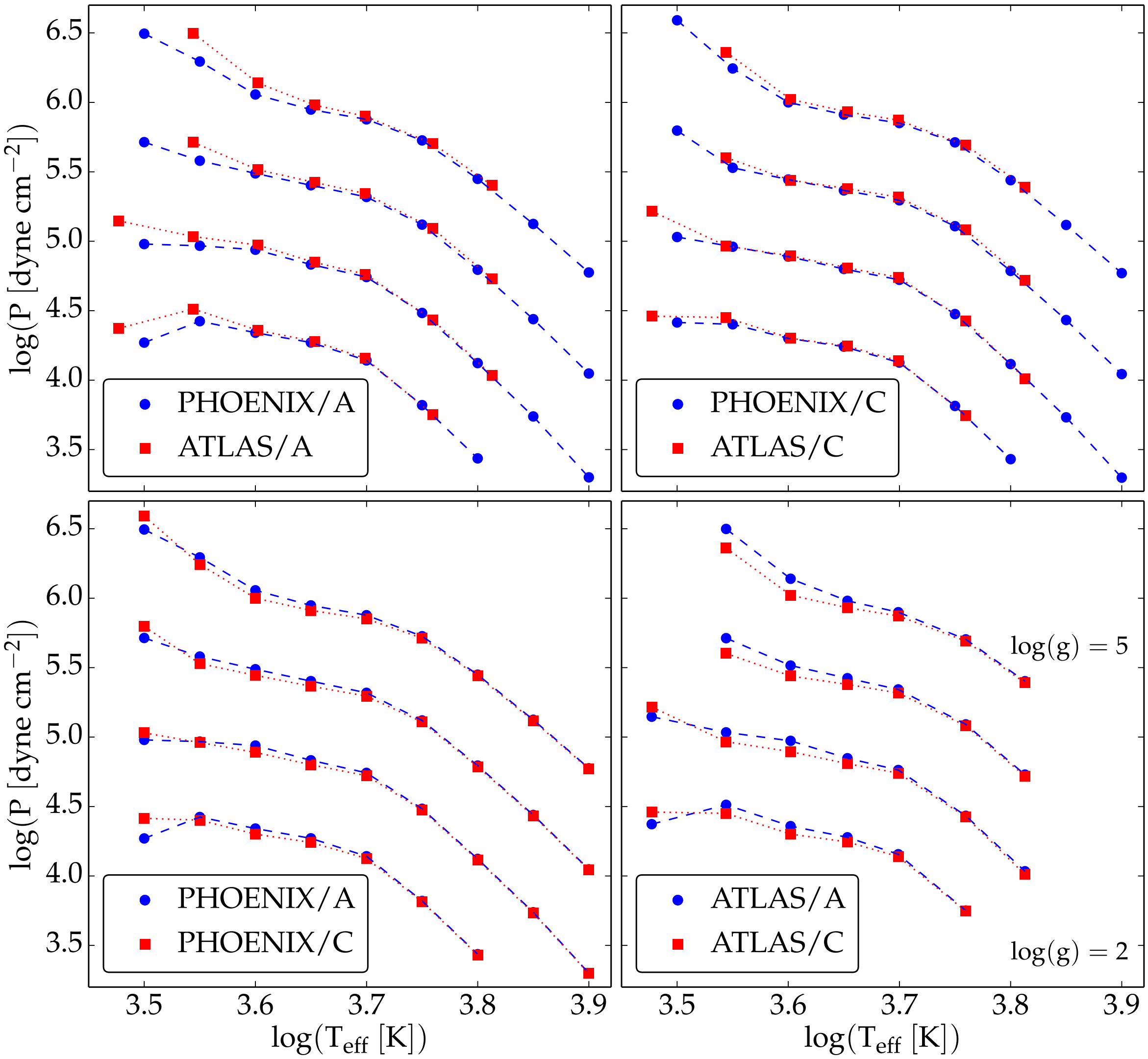

Figure 1. The log of pressure (cgs units) at $T = T_{\rm eff}$ from PHOENIX and ATLAS model atmospheres for cases A and C. The top-left and top-right panels compare PHOENIX and ATLAS for cases A and C, respectively. The bottom-left and bottom-right panels compare cases A and C for PHOENIX and ATLAS, respectively. All panels show models for $\log(g) = 2, 3, 4, 5$ from bottom to top; $\log(g) = 2$ and $\log(g) = 5$ are labelled in the bottom-right panel. All panels have the same dimensions.

our main goal is to discover how well stellar models are able to describe stars at the upper and lower extremes of the light-element abundance distributions. If the models are able to reproduce the observed features in populations A and C, then we are confident that they will perform equally well when applied to population B.

In addition to the published abundances, we have added measurements of carbon in 14 red giants (Yong et al., in preparation) in order to derive representative carbon abundances for populations A and C. Since the spectroscopic measurements do not include Ne, we have set [Ne/Fe] = +0.4 in both populations. We have not included variations in elements heavier than copper because these elements are underabundant to begin with and show only slight variations (not more than 0.2 dex). These heavier elements are expected to have negligible influence on the properties of stellar evolution models in the Hertzsprung-Russell (H–R) diagram and CMD. The results from Yong et al. (in preparation) indicate that the total C+N+O abundance is constant to within the measurement uncertainties (<0.1 dex) across all populations in NGC 6752.

The average abundance ratios adopted for populations A and C are listed in Table 1. A full listing of the abundances used in the paper, including number and mass fractions, is given in Appendix A.

The abundances reported by Yong et al. are based solely on RGB stars in NGC 6752. It is therefore worthwhile to consider whether or not these abundances are appropriate for stars on the MS. Indeed, there is abundant evidence (Carretta et al. 2005; Smith & Briley 2005, 2006; Smith, Briley &, Harbeck 2005) that the CN cycle operating in the H-burning shell, combined with deep mixing as GC stars climb the RGB, influences the surface abundances of carbon and nitrogen while leaving oxygen essentially unchanged.

In the CN-cycle scenario, the MS stars should have a higher carbon abundance, and a lower nitrogen abundance, than what is observed in the red giants while maintaining a constant sum. In the case of population A, carbon and nitrogen differ by ∼0.5 dex (see Table A1). In order to maximize the potential effect of the CN cycle on population A while maintaining a constant sum, we consider a case in which nitrogen is depleted by 2 dex and carbon enhanced

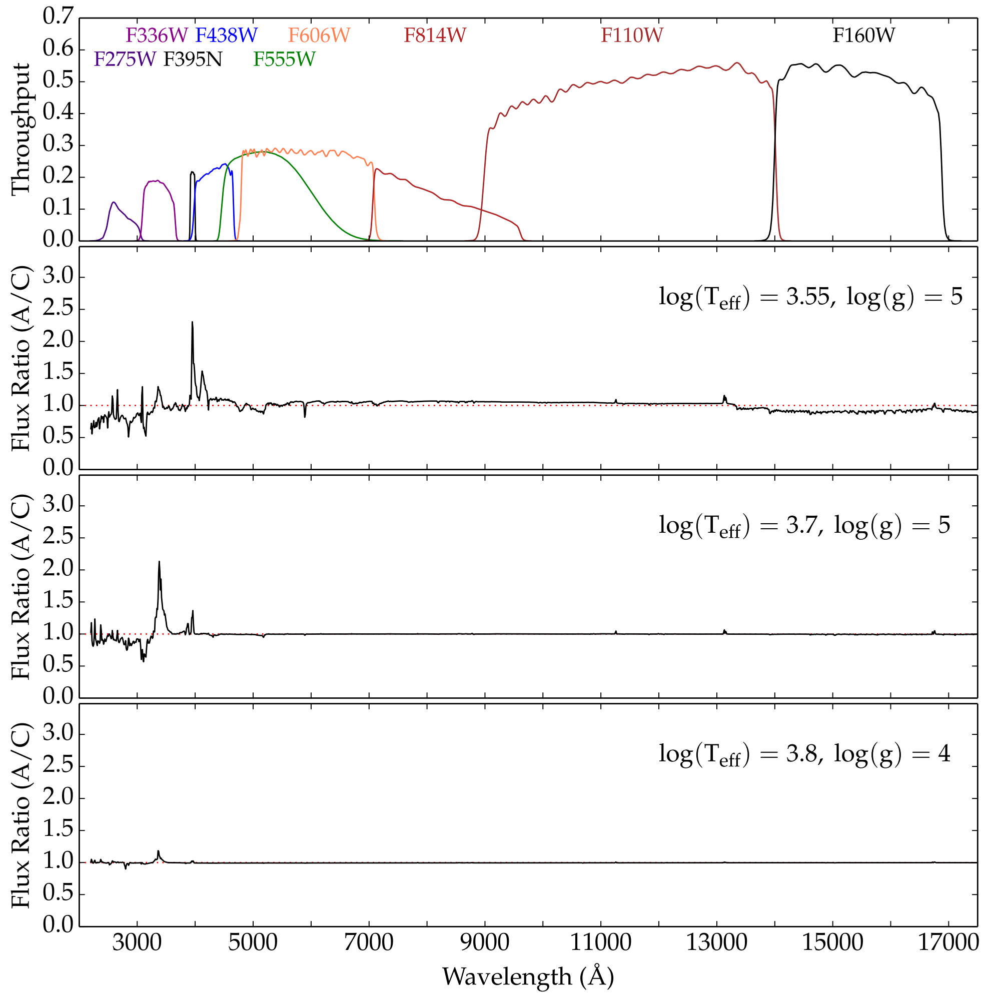

Figure 2. *HST* WFC3 filter throughputs (top) and flux ratios, in the sense of case A over case C, for three pairs of PHOENIX spectra. The wavelength-dependent flux has been smoothed for clarity (see the text for details). The coolest star shows substantial differences for wavelengths shorter than about 5000 Å and longer than about 13 000 Å. The other stars show differences exclusively for wavelengths shorter than 4000 Å.

by 0.15 dex. We shall refer to this case as 'ACN' hereafter. In the case of population C, for which C+N+O is already dominated by nitrogen, any changes due to the CN cycle should be very small because C+N+O will still be dominated by nitrogen, even after some of that nitrogen is converted back to carbon. We have tested this assertion and found that it does not produce any substantial effect in any of the models presented in later sections; it will not be considered further.

Finally, we address the possibility of enhanced helium in population C. A spectroscopic study of horizontal branch (HB) stars in NGC 6752 found no evidence for helium variation ($Y = 0.245 \pm 0.012$) but it was limited to stars on the red side of the HB, which are expected to retain the primordial helium abundance (Villanova, Piotto & Gratton 2009). From careful consideration of colour differences in their full range of *HST* photometry, Milone et al. (2013) estimated an increase in the helium mass fraction of $\Delta Y = 0.03$. In order to quantify the influence of slightly enhanced helium at the level of $\Delta Y = 0.03$, we have computed additional models for population C with $Y = 0.28$; we shall refer to this case as 'CΔY'.

In summary, there are four sets of models that will be described and compared in the following sections:

(i) case A is defined in Table 1 with a helium mass fraction $Y \approx 0.252$;

(ii) case C is also defined in Table 1 with $Y \approx 0.252$;

(iii) case ACN follows the pattern of case A with adjustments to carbon (+0.15 dex) and nitrogen (−2 dex) to account for the CN cycle in red giants while maintaining constant C+N; and

(iv) case CΔY follows case C with an enhancement to helium such that $\Delta Y = 0.03$.

3 STELLAR ATMOSPHERES MODELS

The abundance profiles described in Section 2 and listed in Appendix A were used to construct model atmosphere structures and synthetic spectra with two different codes.

3.1 ATLAS and SYNTHE

The ATLAS models for cases A and C were computed with the ATLAS12 model atmosphere code, part of the Kurucz lineage of atmosphere routines (Kurucz 1970, 1993), ported to Linux by Sbordone et al. (2004). The grid of models covers $\log(g)$ = 2, 3, 4, and 5 and $T_{\rm eff}$ = 3500, 4000, 4500, 5000, 5750, and 6500 K. ATLAS12 employs

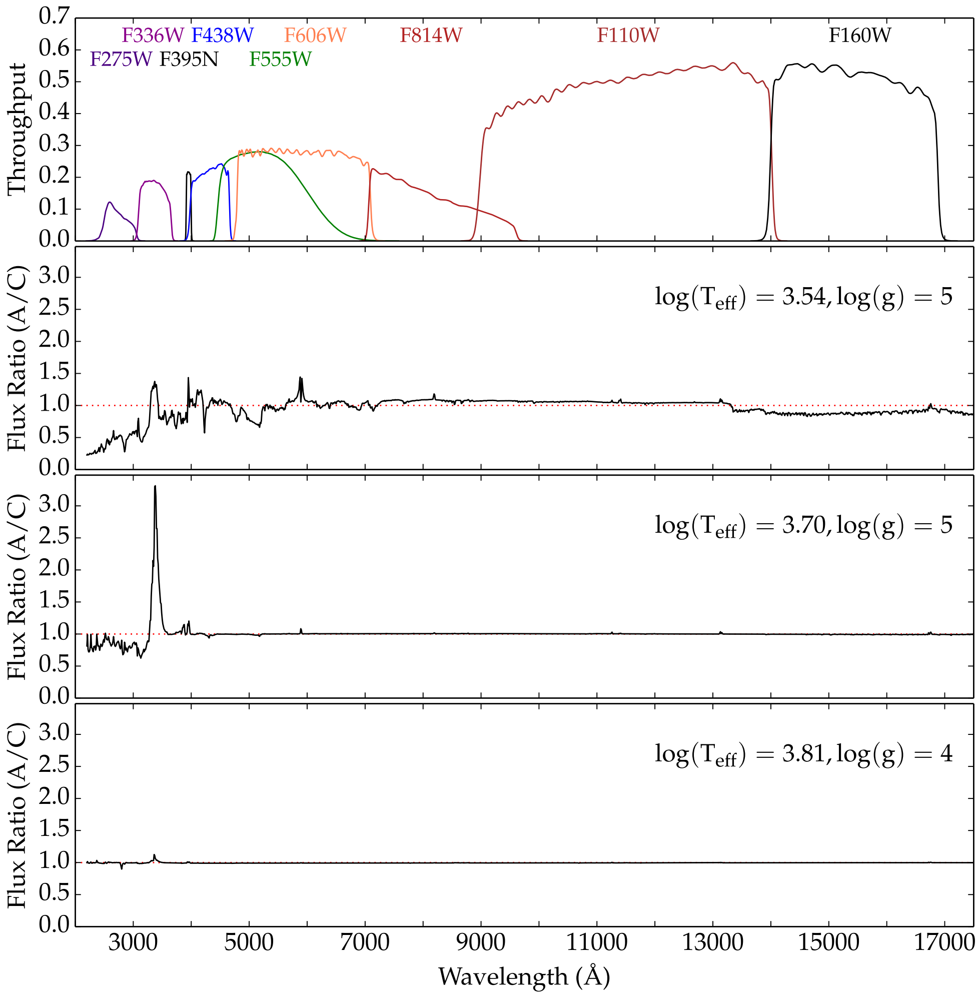

Figure 3. *HST* WFC3 filter throughputs (top) and flux ratios, in the sense of case A over case C, for three pairs of ATLAS/SYNTHE models. The wavelength-dependent flux has been smoothed for clarity. The dimensions of each panel are identical to those in Fig. 2. The results are mostly similar to the PHOENIX models shown in Fig. 2 but the ATLAS/SYNTHE models show stronger differences in the optical spectrum for the coolest star.

the opacity-sampling technique to construct model atmospheres. These are plane-parallel and assume local thermodynamic equilibrium (LTE). A microturbulent velocity of 2 km s^{-1} was adopted for all of the models. Synthetic spectra were computed with SYNTHE (Kurucz & Avrett 1981) at a resolution of $R = 500\,000$ from 1000 to 30 000 Å. The latest atomic line lists (kindly provided by R. Kurucz) were used, as were molecular line lists for H_2O, TiO, FeH, CrH, CaH, C_2, CN, CH, NH, SiO, SiH, OH, MgH, CO, and H_2.[1]

3.2 PHOENIX

A grid of model atmospheres and synthetic spectra computed using the PHOENIX code version discussed by Hauschildt, Allard & Baron (1999a) and Hauschildt et al. (1999b) with updates described by Ferguson et al. (2005). The individual models are plane-parallel, assume LTE, and have a microturbulent velocity of 2 km s^{-1}. The resolution of the synthetic spectra differs by region; the one relevant to this study is 0.2 Å between 1000 and 20 000 Å. Grids of atmospheres and synthetic spectra were generated for cases A and C with effective temperatures from $\log(T_{\rm eff}) = 3.50$ (∼3100 K) to 3.90 (∼8000 K), in steps of 0.05 dex and values of $\log(g)$ from 2.0 to 5.5 in steps of 0.5 dex. Additional models were computed for cases ACN and CΔY for the full range of $\log(T_{\rm eff})$ given above, at $\log(g) = 5$, to provide comparisons with cases A and C for conditions appropriate for stars on and near the MS.

3.3 Comparisons

The model atmosphere structures differ only slightly between cases A and C, with departure growing as temperature decreases. Fig. 1 shows the photosphere pressure (extracted at $T = T_{\rm eff}$) from both PHOENIX and ATLAS models for a range of $\log(g)$ and cases A and C. The pressure is used as the surface boundary condition in the stellar evolution models, see Section 4. The upper panels of Fig. 1 compare PHOENIX and ATLAS pressures for case A (left) and case C (right); the bottom panels compare cases A and C from PHOENIX (left) and ATLAS (right). The upper panels indicate that PHOENIX and ATLAS yield very similar pressures except for the lowest temperature point in the ATLAS grid. The lower panels indicate that cases A and C give essentially the same pressures above 5000 K ($\log(T_{\rm eff}[{\rm K}]) = 3.7$). Between 3500 and 5000 K, case A has consistently higher pressures; below 3500 K, the situation reverses and case C has the higher pressure.

[1]The line lists are currently undergoing a major update. Quantitative results based on these models, particularly in the UV, are subject to change.

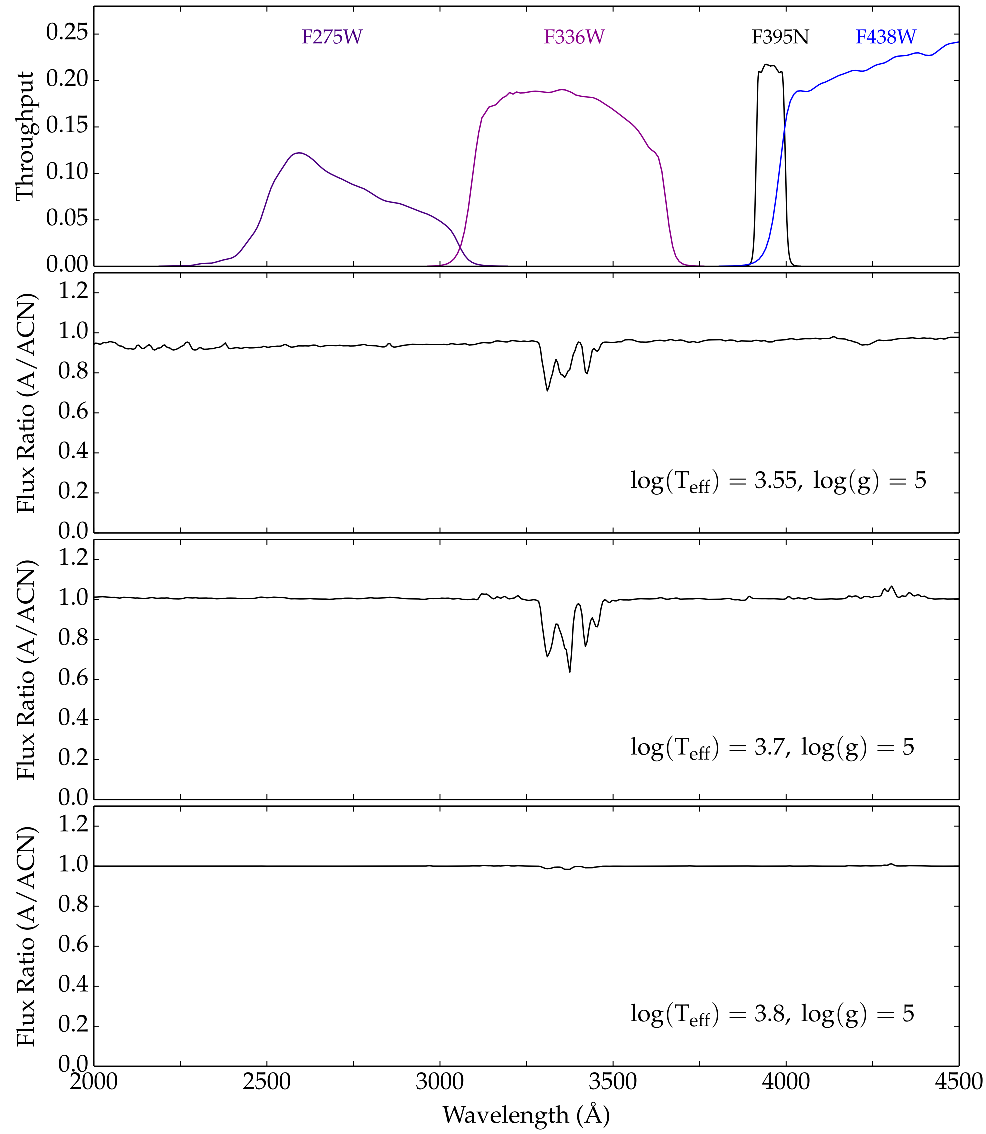

Figure 4. *HST* WFC3 filter throughputs (top) and flux ratios, in the sense of case A to case ACN, for three PHOENIX models. The wavelength-dependent flux has been smoothed for clarity. Flux differences due to CN cycling on the RGB appear mostly in the *F*336*W* filter. Note that the *x*- and *y*-axes show smaller regions than in Figs 2 and 3.

The difference in pressure for the coolest stars is due to differences in the molecular composition which, in turn, is driven by chemical equilibrium as set by the respective equations of state. Difference in composition leads to difference in opacity and, ultimately, to difference in the atmosphere structure.

Fig. 2 shows the throughput of several *HST* WFC3 filters, in the top panel, followed by the ratio of the fluxes (measured in erg cm^{-2} s^{-1} Å^{-1}) from PHOENIX synthetic spectra for cases A and C at fixed temperatures and gravities. The flux is plotted every 10 Å and has been smoothed with a 3 Å Gaussian filter for improved clarity. The temperatures and gravities are representative of points along the MS and chosen to correspond, as closely as possible, to models in the ATLAS/SYNTHE grid. Fig. 3 is the equivalent of Fig. 2 for the ATLAS/SYNTHE grid; the SYNTHE spectra were smoothed in the same way as the PHOENIX spectra.

Figs 2 and 3 both show, for the coolest temperature, that there are significant differences in the fluxes between cases A and C below 5000 Å and above 13 000 Å. For the hotter temperatures, the differences are restricted to wavelengths shorter than 4000 Å. The difference in the coolest models' flux ratio in the near-IR is due to suppressed H_2O absorption because of the reduction of oxygen in case C compared to case A. SiO absorption in the UV is an important factor in the flux ratio bluewards of 3000 Å. NH is responsible for the peak near 3300 Å.

The contribution of CN in the coolest models shown in Figs 2 and 3 is negligible because the majority of carbon is locked up in CO; this is true in cases A and C because oxygen outnumbers carbon in both cases. In this way, the MS differs from the RGB, where CN variations have been observed for many years (Freeman & Norris 1981).

Fig. 4 shows the flux ratio of cases A and ACN, similar to Figs 2 and 3 and with the same smoothing applied, though the differences are much more restricted in this case. The species responsible for the only significant variations in Fig. 4 is NH. We were able to

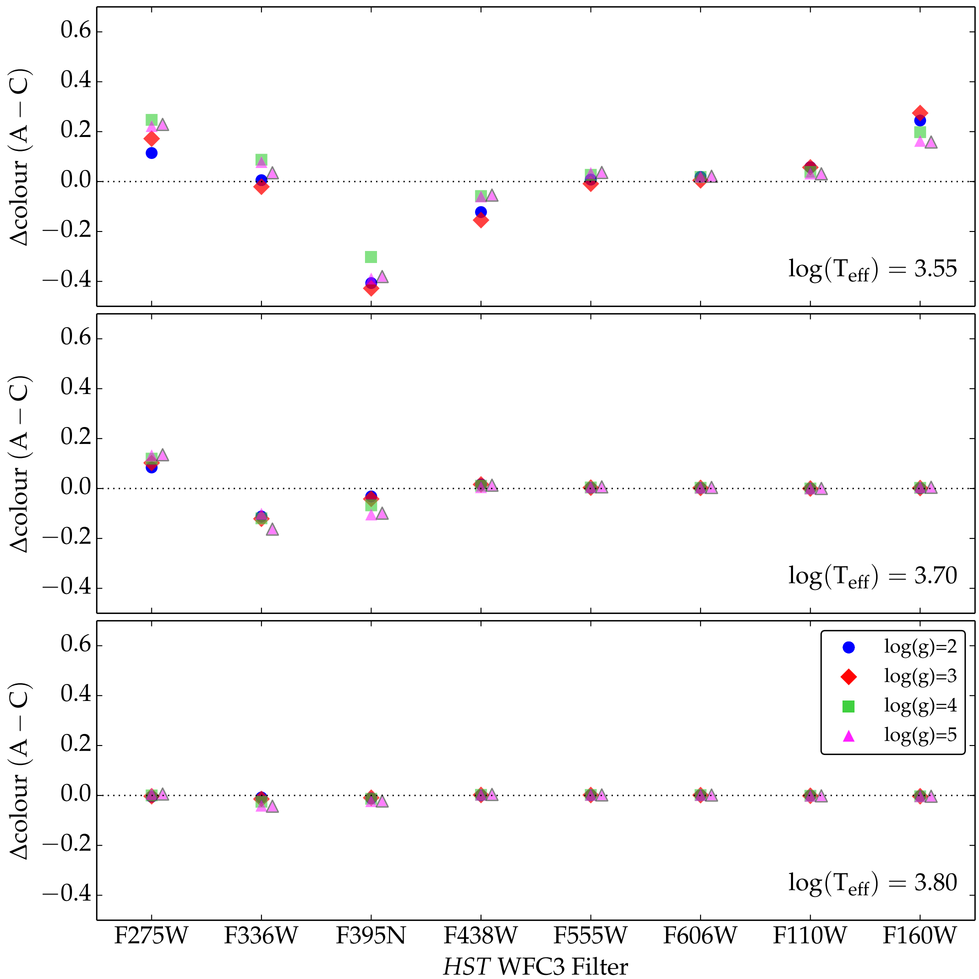

Figure 5. Colour difference, defined with respect to *F*814*W*, between cases A and C for the PHOENIX synthetic spectra shown in Fig. 2. Colour difference between cases ACN and C, for $\log(g) = 5$ only, are shown offset slightly to the right and with a black outline. Case ACN is only relevant in *F*336*W* as should be evident from Fig. 4.

verify this by computing additional PHOENIX models without NH for the same abundances and physical conditions: the flux ratio for these models is flat (ratio = 1) through the same wavelength region. Whereas the differences between cases A and C will alter synthetic photometry in UV and IR filters, the difference between cases A and ACN will only modestly influence the *F*336*W* filter. For the MS stars considered here, the difference between cases A and ACN in the *F*336*W* filter amounts to, at most, 0.1 mag at about 4200 K. The difference decreases to less than 0.02 mag above 5500 K and below 3000 K. In both *F*275*W* and *F*438*W*, the same models never differ by more than 0.02 mag.

The flux ratios shown in Figs 2 and 3 will have a measurable influence on the bolometric corrections, hence colours, derived from the synthetic fluxes. Figs 5 and 6 show the colour difference between cases A and C for a selection of nine *HST* WFC3 filters. These figures are modelled after, and should be compared with, figs 17 and 18 of Milone et al. (2013) where they are used to demonstrate the separation between sequence in different colours. Fig. 5 also shows, offset to the right, the colour difference between cases ACN and C for $\log(g) = 5$ only. The temperatures shown are the same as in Figs 5 and 6, respectively, for a range of surface gravities. In Figs 5 and 6, Δcolour refers to the colour derived from the case A synthetic spectrum minus the colour derived from the case C synthetic spectrum for the same physical parameters. The colours are defined with respect to *F*814*W* as $M_{\rm Filter} - M_{F814W}$.[2]

Both Figs 5 and 6 indicate that the warmer spectra (the two bottom panels) show colour differences measured in hundredths of magnitudes for the optical and IR filters; the only significant differences for these spectra are in the UV. For the coolest spectra, the colour differences are more substantial for all filters except *F*555*W* and *F*606*W*. The effect of accounting for CN-cycle modifications to the surface abundances results in non-negligible differences only to *F*336*W*, consistent with Fig. 4.

[2]We acknowledge that what is shown here from the models is really a difference in magnitude – not colour – for a given filter, taken at a fixed *F*814*W* magnitude. However, we have chosen to present it as a colour difference in accordance with Milone et al. (2013). The main reason is that this measurement would be done in terms of colour at fixed magnitude in an observed CMD.

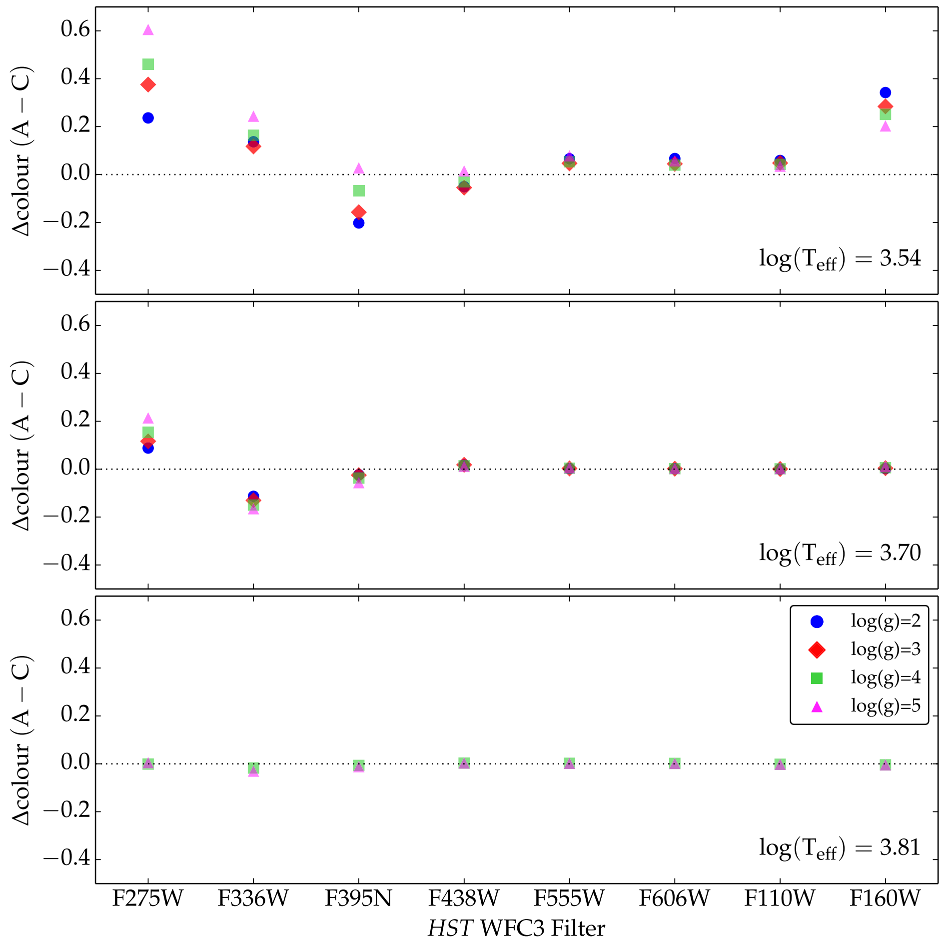

Figure 6. Colour difference, defined with respect to $F814W$, between cases A and C for the SYNTHE synthetic spectra shown in Fig. 3. The dimensions of each panel are the same as in Fig. 5.

4 STELLAR EVOLUTION MODELS AND ISOCHRONES

Stellar evolution models were computed with the Dartmouth Stellar Evolution Program (DSEP), which has been configured to self-consistently account for specific chemical abundance patterns in the nuclear reactions, equation of state, low- and high-temperature opacities, and surface boundary condition (Dotter et al. 2007b). The model atmospheres described in Section 3 were used to derive the surface boundary condition, the photosphere pressure, at the point in the atmosphere where $T = T_{\mathrm{eff}}$ for each composition and from each atmosphere code (see Fig. 1 and the related text).

All details of the code remain as stated by Dotter et al. (2007a, 2008), and we list here only those elements of the code most relevant to this study: DSEP uses the FreeEOS equation of state,[3] high-temperature opacities from OPAL (Iglesias & Rogers 1996), and low-temperature opacities from PHOENIX (Ferguson et al. 2005). The opacities were computed for the abundance patterns described in Section 2 (see Appendix A for full details).

The Rosseland mean low-temperature opacities differ between cases A and C by no more than 2 per cent above 5500 K; since the stellar evolution models cooler than 5500 K have substantial convective envelopes, and use model atmosphere boundary conditions, the influence of the low-temperature opacities is minimal. The same goes for the high-temperature opacities, where the largest – though still quite modest – difference occurs around 10^6 K.

Stellar evolution tracks with masses from 0.2 to 0.8 $\mathrm{M}_{\odot}$ were computed starting from the fully convective pre-MS and ending at a point suitable for the construction of isochrones with ages appropriate for GCs, namely 10–14 Gyr. The evolutionary tracks were transformed into isochrones in the same manner as those of the Dartmouth Stellar Evolution Database (Dotter et al. 2007a, 2008) and then converted to observable magnitudes by interpolation in bolometric correction tables that were derived from the synthetic spectra described in Section 3.

Fig. 7 shows 13 Gyr isochrones computed using the surface boundary condition from PHOENIX models (left) and ATLAS models (centre) for cases A, C, and CΔY (the last of which uses the same boundary condition as case C). The right-hand panel shows the temperature difference at fixed luminosity between different cases. The plot shows similar behaviour in both panels: case A and case C overlap almost perfectly from the base of the RGB through the MS turnoff (MSTO) and down the MS until T_{eff} reaches about 4500 K. Below 4500 K, corresponding to $\log(L/\mathrm{L}_{\odot}) \sim -1$, the onset of molecules in the atmospheres begins to push cases A and C apart with A remaining slightly hotter – but never by more than about 50 K – than C down to the extent of the models shown (0.2 $\mathrm{M}_{\odot}$). The PHOENIX models show a smaller separation than the ATLAS models; this can be traced back to the difference in surface pressures seen in Fig. 1. The CΔY isochrone is consistently hotter than the C

[3] http://freeeos.sourceforge.net

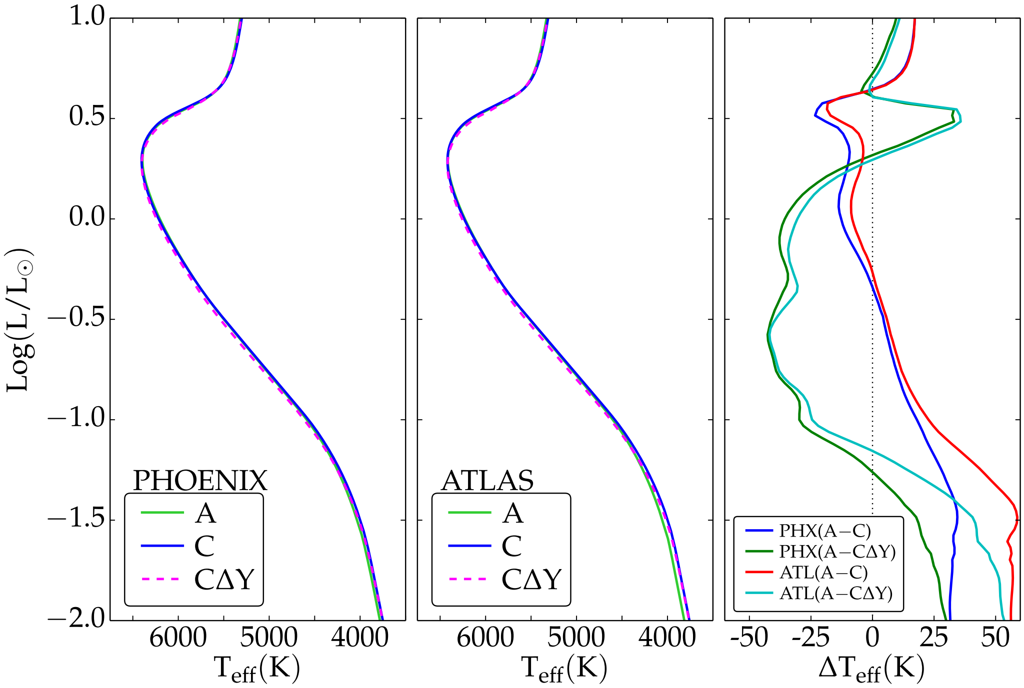

Figure 7. 13 Gyr isochrones computed for cases A, C, and CΔY with atmosphere boundary conditions from PHOENIX (left) and ATLAS (centre). The dimensions of both panels are the same. The right-hand panel shows the temperature difference between cases A and C and A and CΔY at fixed luminosity. Here, PHOENIX is abbreviated to PHX and ATLAS to ATL. Noticeable differences between A and C appear only as $T_{\rm eff}$ falls below 5000 K and molecules become important in the atmosphere. CΔY shows the characteristic appearance of stellar models with slightly enhanced helium: marginally hotter along the MS with a steeper slope through the subgiant branch.

isochrone below the MSTO and above the molecular regime, which is typical behaviour for slightly helium-enhanced stellar evolution models, but the difference is only at the level of 50 K.

The similarity evident in Fig. 7 indicates that the observed differences in various colour combinations are due to the influence of abundance variations on the stellar spectra with only a modest contribution from the difference in $T_{\rm eff}$ on the lower MS. Fig. 7 reiterates the point already made by Pietrinferni et al. (2009) that the influence of light-element variations on isochrone ages is negligible so long as the total C+N+O content is constant among the different stellar populations.

Isochrones transformed into five broad-band CMDs from the *HST* WFC3 (Vegamag) photometric system are presented in Fig. 8 for bolometric corrections from PHOENIX models and Fig. 9 for ATLAS/SYNTHE models. Qualitatively, each CMD shows the same behaviour from the PHOENIX and ATLAS/SYNTHE models. In the UV and blue filters, there are substantial differences between cases A and C, in the optical CMDs the differences are minimal, and the near-IR cases A and C separate below the ‘knee’ on the lower MS. More detailed discussion of some of these features will be given in Section 5 where the isochrones are compared with the *HST* photometry of Milone et al. (2013).

5 COMPARISONS WITH *HST* PHOTOMETRY

This section will demonstrate the extent to which the isochrones presented in Section 4 are able to match the *HST* photometry of NGC 6752 by Milone et al. (2013) along the MS. Throughout, we have adopted an isochrone age of 13 Gyr for both populations, a true distance modulus of $(m-M)_0 = 13.13$ (Harris 1996, specifically the 2010 revision), and a reddening value of $E(B-V) = 0.0485$ (Schlafly & Finkbeiner 2011). We have used the Cardelli, Clayton & Mathis (1989) extinction curve with the adopted reddening value and $R_{\rm V} = 3.1$, corresponding to $A_{\rm V} = 0.15$, to derive the extinction along with the bolometric correction in each bandpass for each synthetic spectrum.

5.1 UV and blue CMDs

The comparisons begin with $F275W - F336W$ (upper panels) and $F336W - F410M$ (lower panels) in Fig. 10. In both rows of Fig. 10, the left-hand panel shows the ATLAS isochrones with SYNTHE bolometric corrections and the right-hand panels show the PHOENIX isochrones. The data are shown as Hess diagrams in order to better display the split sequences.

In the $F275W - F336W$ CMD, both sets of isochrones provide a reasonable description of data from the turnoff to about 2 (ATLAS/SYNTHE) or 3 (PHOENIX) mag fainter before they diverge bluewards of the data. The separation is more dramatic in the ATLAS/SYNTHE case. Comparison of the two sets of isochrones with the Hess diagram shows that the separation between populations A and C increases slowly from $\Delta(F275W - F336W) \sim 0$ at the turnoff to $\Delta(F275W - F336W) = 0.2$–$0.3$ at the limit of the diagram ($F275W = 23$). While the isochrones do not match the data in an absolute sense, the relative separation in $F275W - F336W$ at fixed magnitude is, at least qualitatively, reproduced by both sets of models.

In the $F336W - F410M$ CMD, the isochrones stay within the envelope of the data points for almost the full extent of the CMD shown in Fig. 10. The separation between the populations within 2 mag of the turnoff is reproduced by the models. In this case, the ATLAS/SYNTHE models give an accurate representation of the data from the base of the RGB to the lower limit shown at $F410M = 23.5$. Both sets of models predict that the sequences should cross at

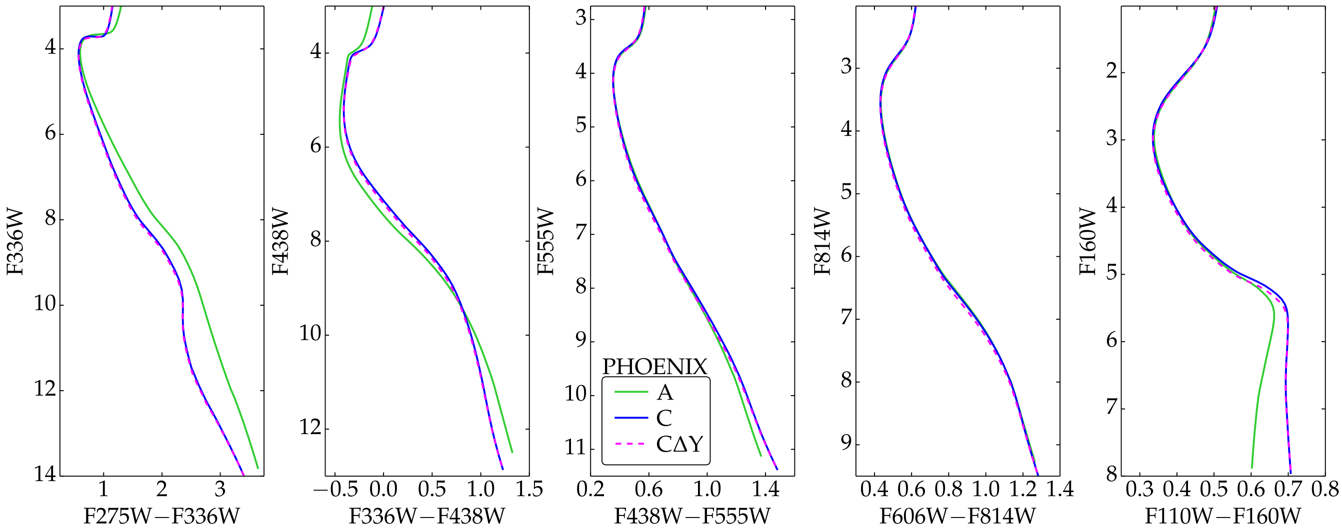

Figure 8. The 13 Gyr PHOENIX isochrones shown in Fig. 7 with *HST* WFC3 bolometric corrections from the PHOENIX synthetic spectra. The key in the middle panel applies to all.

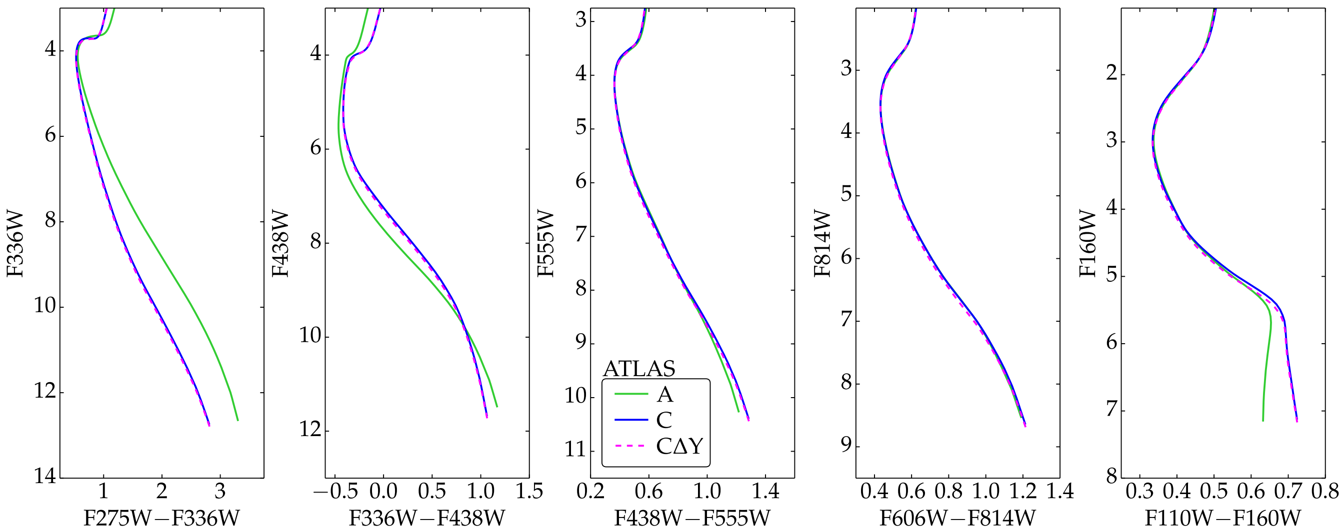

Figure 9. Equivalent to Fig. 8 for the 13 Gyr ATLAS isochrones with bolometric corrections from the SYNTHE spectra. The dimensions of each panel are the same as the corresponding panel in Fig. 8; the models end at brighter magnitudes than those in Fig. 8 because the SYNTHE spectra are limited to $T_{\mathrm{eff}} \geq 3500$ K. The key in the middle panel applies to all.

*F*410*M* ∼ 23 but, unfortunately, the photometric errors are too large at this point, and the data run out just below, to verify the model prediction.

There are a variety of reasons why cool star models may be discrepant with the data in UV and blue spectral regions. These include missing opacity from atoms and molecules, neglect of non-LTE effects, and phenomenological treatment of inherently 3D physics in stellar atmosphere (e.g. convection and microturbulence). Suffice it to say that, while the models leave room for improvement in an absolute sense, both the general trends and also the relative difference between cases A and C are consistent with the observations.

5.2 Optical and near-IR CMDs

Sbordone et al. (2011) pointed out that the influence of abundance variations on synthetic spectra and photometry are significant in the UV and blue but leave the optical largely untouched. Figs 8 and 9 suggest that the most prominent CMD in recent *HST* GC age studies, *HST* Advanced Camera for Surveys (ACS) *F*606*W* − *F*814*W* (Sarajedini et al. 2007; Anderson et al. 2008), is insensitive to light-element abundance variations provided that C+N+O remains constant.

Fig. 11 compares the ACS photometry (Anderson et al. 2008) with the isochrones in the *F*606*W* − *F*814*W* CMD. It should be clear from this comparison that there is essentially no difference between populations A and C in this CMD and that, even with a small Δ*Y* between populations A and C, this is perhaps the safest CMD in which to perform GC age analyses because it is the least sensitive to the photometric manifestation of light-element variations.

The synthetic spectra by Sbordone et al. (2011) extended only to 10 000 Å and, therefore, the near-IR filters were excluded from their analysis. Meanwhile observations of NGC 2808 (Milone et al. 2012) and M4 (Milone et al. 2014) show that the MS of both clusters fans out below the ‘knee’ in the *HST* WFC3/IR *F*110*W* − *F*160*W* CMD. The same feature has also been observed in 47 Tuc by Kalirai et al.

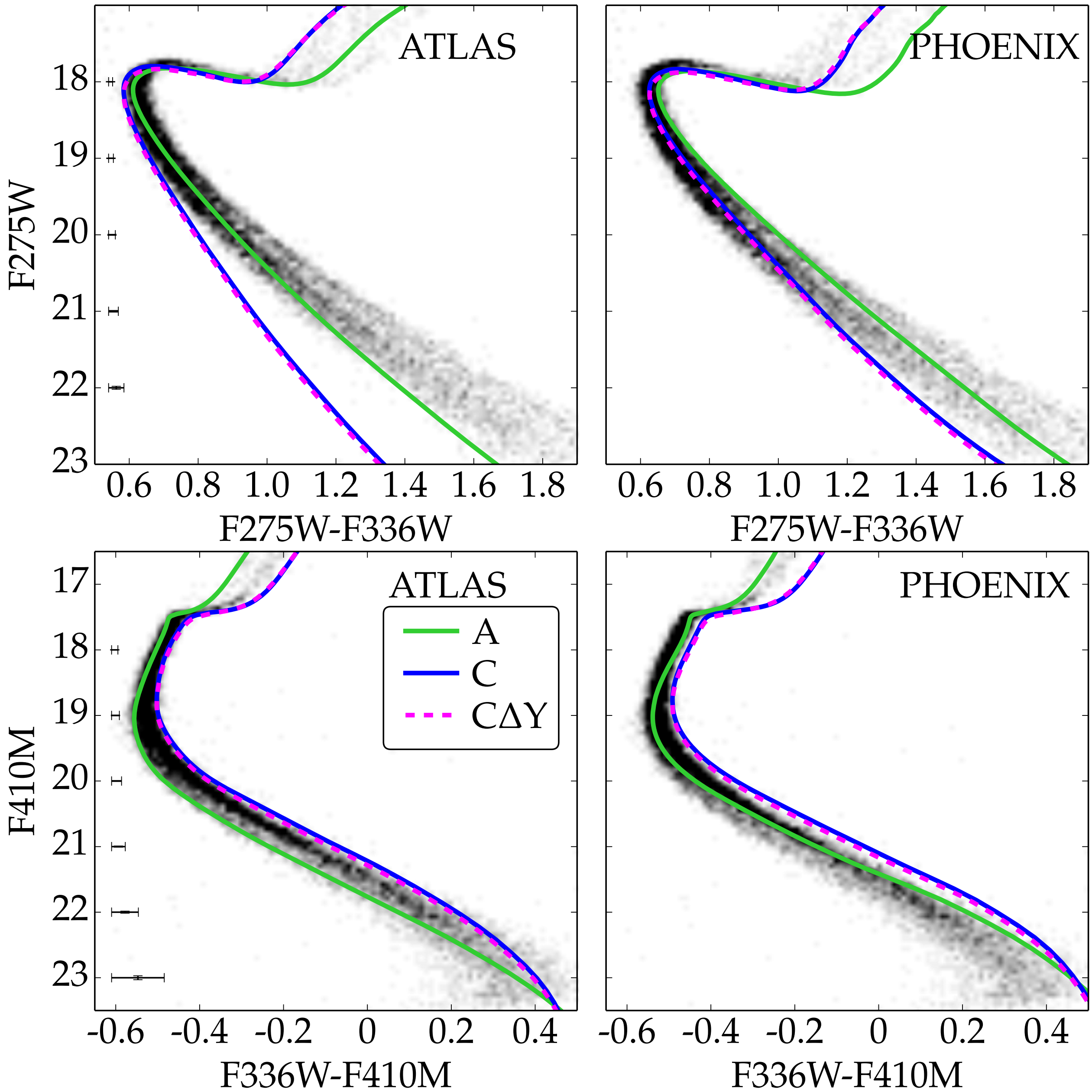

Figure 10. The top row shows the $F275W - F336W$ CMD compared with ATLAS isochrones (left) and PHOENIX isochrones (right). The bottom row shows the analogous panels for the $F336W - F410M$ CMD. Typical photometric errors are shown on the left edge of the left-hand panel in each row.

(2012). The broadening of the lower MS is attributed to variation in absorption by water, primarily in the $F160W$ filter (Milone et al. 2012, 2014). This conclusion is fully supported by the material presented in Section 3.

We plot the isochrones on top of the *HST* WFC3/IR CMD in Fig. 12. The CMD is based on the same data as presented by Milone et al. (2013) but, unlike in Milone et al. (2013) where only stars found in all bandpasses were shown, we have included all stars that were measured in the near-IR observations. The models clearly indicate that the sequences should split just above the knee. Population A should have bluer $F110W - F160W$ colours than population C below the knee. This is consistent with the flux ratios of the coolest models shown in Figs 2 and 3.

The comparison between models and data in Fig. 12 suggests that the near-IR CMD can provide an estimate of oxygen variation within a GC such as NGC 6752 provided that self-consistent models for the appropriate metallicity, and with a range of oxygen, are available. Furthermore, a proper accounting of the photometric errors in the data is required to distinguish between a spread in the MS due to abundance variation or increasing photometric error. The models show an obvious trade-off between the location at which the spread is measured and the sensitivity of the near-IR colour. In the case of NGC 6752 shown here, the spread increases from nearly zero at the knee to almost 0.1 in colour about 2 mag below the knee. This technique may prove a useful first step in studying oxygen variation in GCs which have, for example, few bright red giants or significant extinction: either of which would complicate a proper spectroscopy analysis. This claim is supported by the comparison of M4 and NGC 2808 by Milone et al. (2014, section 4). It is worthwhile to consider the value of this technique in light of the

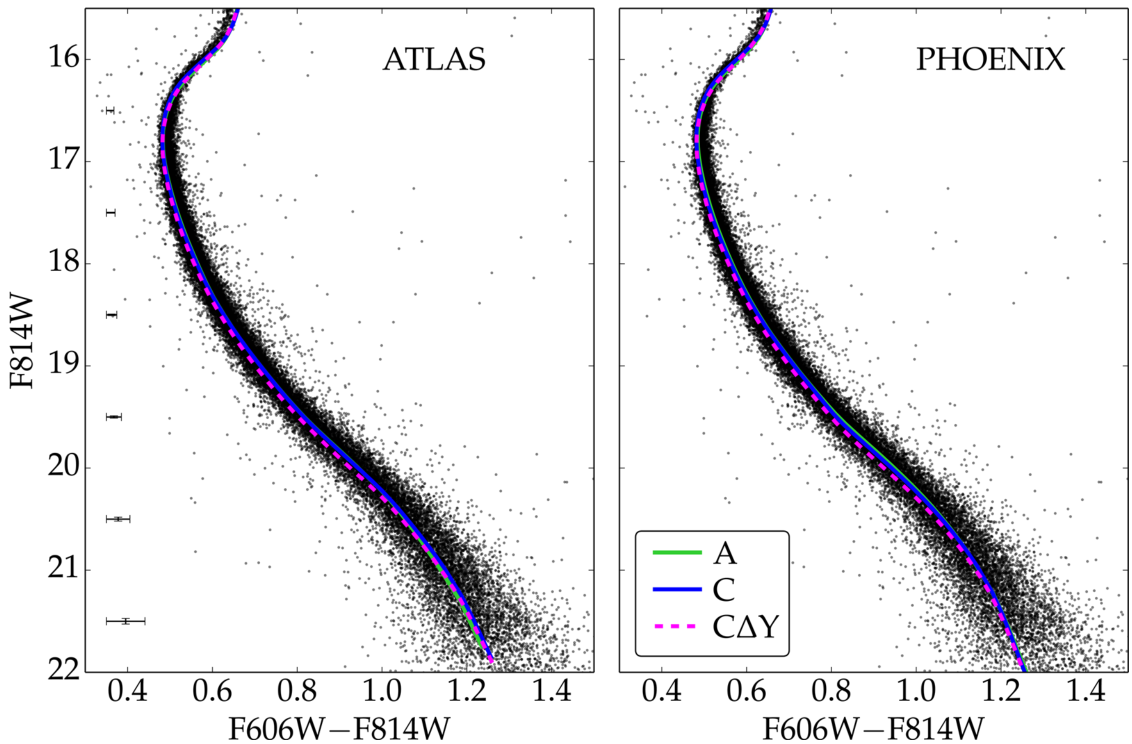

Figure 11. Isochrones from populations A and C compared to the *HST* ACS *F*606*W* − *F*814*W* CMD (Sarajedini et al. 2007; Anderson et al. 2008). Typical photometric errors are shown on the left edge of the left-hand panel. Both sets of models show no obvious difference except that the helium-enhanced models are very slightly hotter along the MS.

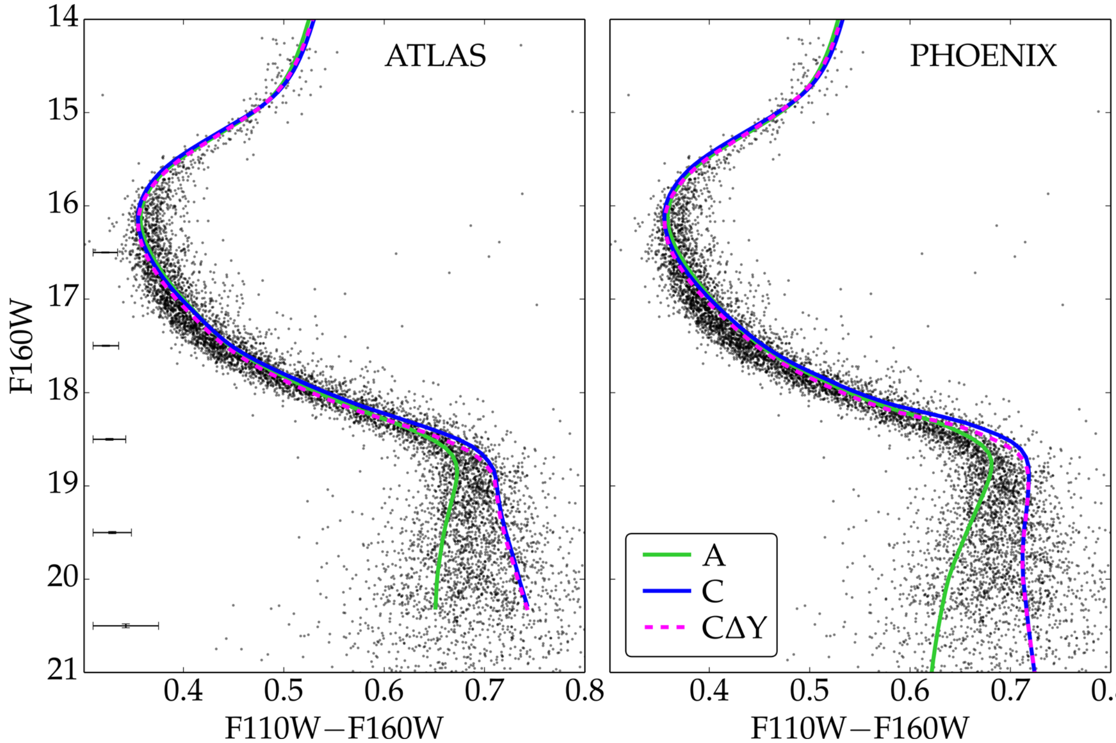

Figure 12. Isochrones for populations A and C compared to the *HST F*110*W* − *F*160*W* CMD. Typical photometric errors are shown along the left edge of the left-hand panel. The separation of populations A and C is evident in both diagrams, with both sets of models showing population A bluer than C below the MS knee.

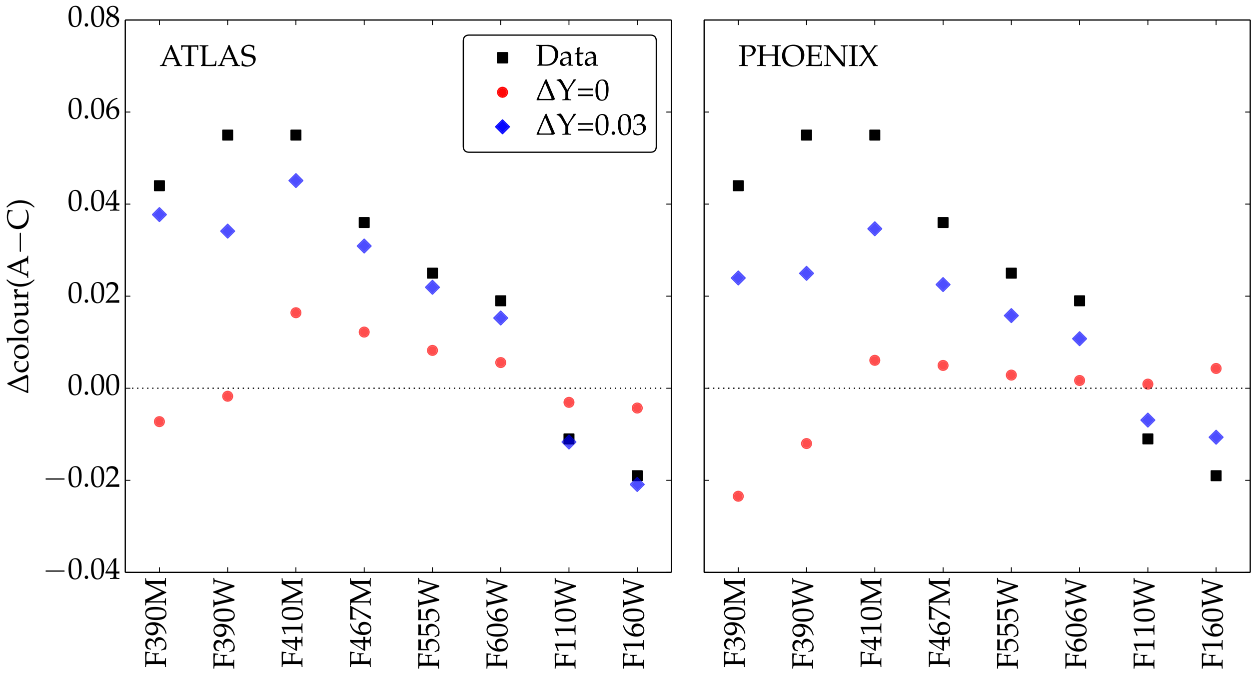

Figure 13. The colour differences between cases A and C in a variety of filters at $F814W = 18.5$ for ATLAS/SYNTHE isochrones (left) and PHOENIX isochrones (right). These are compared with the equivalent measurement of populations A and C by Milone et al. (2013). The plot demonstrates the influence of enhanced helium on the relative colours of the two populations.

current capabilities of *HST* WFC3/IR as well as the advent of the *James Webb Space Telescope*.

5.3 Helium abundance variation from multiband photometry of the MS

Milone et al. (2013) used the broad wavelength coverage of the *HST* photometry, along with the ATLAS and SYNTHE codes, to generate model atmospheres and synthetic spectra for the stellar populations in NGC 6752. They compared the observed colour difference between populations A and C at fixed $F814W$ magnitude in several colours with synthetic spectra. The synthetic spectra for population C included varying helium abundance (up to $Y = 0.29$) and Milone et al. (2013) used these to estimate the helium abundance of population C: an enhancement above population A by $\Delta Y \sim 0.03$.

The same analysis can be performed with the isochrones at the location on the MS adopted by Milone et al., $F814W = 18.5$. To do so, the magnitudes of eight filters considered by Milone et al. (2013, see their fig. 9) were extracted from the isochrones at $F814W = 18.5$. The colour difference between cases A and C, given by $(\text{Filter} - F814W)_A - (\text{Filter} - F814W)_C$, was computed for each filter considered; the same was done for the difference between cases A and CΔY. The results of this exercise are plotted in Fig. 13, where the two variants of case C are identified by their level of helium enhancement relative to case A; this is done to highlight the influence of helium abundance on the MS colours at fixed $F814W$ magnitude.

The UV filters have been excluded from Fig. 13 because they are the most sensitive to variations in light elements other than helium. However, starting with the $F390M$ filter and extending redwards, the ATLAS/SYNTHE isochrone for case CΔY ($\Delta Y = 0.03$) provides a good match to the observations. This should not come as a surprise because the level of helium enhancement estimated by Milone et al. (2013) was based on comparisons of their data with ATLAS/SYNTHE models. Nor can it be taken as an independent confirmation of that result because our case CΔY was chosen based on the estimate from Milone et al. (2013). Having said all that, the left-hand panel of Fig. 13 is a confirmation that some degree of helium enhancement is required to match the observation because the case C isochrone ($\Delta Y = 0$) shows considerably less variation relative to case A, which is inconsistent with the data.

The right-hand panel of Fig. 13 provides an important check on this technique. Whereas the ATLAS/SYNTHE isochrones produced in this study are consistent with the estimate of helium enhancement using atmosphere models from (essentially) the same codes, the PHOENIX models would require a larger helium enhancement (by a factor of $\lesssim 2$) in population C in order to match the observations. We conclude that the use of multiband photometry to estimate helium variation among different populations in GCs is a viable technique but that the resulting ΔY depends on the model atmospheres employed. More work in this direction is certainly called for.

6 CONCLUSIONS

In the context of multiple populations in GCs, this study represents the first successful confrontation between the best available observational material, both photometry and spectroscopy, and self-consistent theoretical modelling of stellar interiors and atmospheres.

This study presents self-consistent stellar atmosphere and evolution models directly addressing the presence of multiple stellar populations on the MS of NGC 6752. The abundances adopted in the models are taken from spectroscopic analyses. Two sets of model atmospheres and synthetic spectra were computed using ATLAS/SYNTHE and PHOENIX in order to reveal the differences that may arise from adopting one set of atmosphere models or another.

ATLAS/SYNTHE and PHOENIX spectra differ somewhat, particularly in the UV, which translates into noticeable differences in the UV and blue synthetic CMDs. It is not obvious that one set of models matches the *HST F*275*W* data better than the other, though the ATLAS/SYNTHE models perform better in $F336W - F410M$. Further improvements to the model atmospheres and synthetic spectra that directly address the UV would be welcome.

The combination of a good match between the models and the optical CMDs and the fact that multiple populations are essentially indistinguishable in the optical CMDs recommends the use of optical CMDs for GC age analyses. This point does not extend to those GCs whose optical CMDs reveal the presence of multiple populations (e.g. NGC 1851; Milone et al. 2008).

The spread of the lower MS in the near-IR CMD, caused by water absorption, provides a useful probe of the range of oxygen variation in the cluster provided that photometric errors are accounted for and stellar models for the appropriate compositions are used. PHOENIX and ATLAS/SYNTHE models predict essentially the same behaviour within ∼1 mag of the 'knee' though the ATLAS/SYNTHE models trace the knee itself better. This feature represents a relatively inexpensive way to estimate the level of oxygen variation in a GC.

The models support the use of multiband photometry to estimate helium variations among the different populations in NGC 6752 and other, similar GCs using the technique developed by Milone and collaborators. However, it is important to note that the estimate of helium variation is model dependent; ATLAS/SYNTHE models show a stronger sensitivity to helium variation than PHOENIX models.

The next step in this project will be to extend the current analysis to the RGB and the HB. The Milone et al. (2013) photometry covers the full extent of the RGB and HB stars and, through detailed modelling, we intend to study the complex relationship between light-element abundance variations (including helium) and cumulative mass-loss on the RGB as manifested in the HB morphology.

The phenomenon of multiple stellar populations in GCs represents a major challenge to our understanding of stellar evolution and nucleosynthesis. Successfully reproducing the observed characteristics at all evolutionary stages, from the MS through the RGB and on to the HB, would serve as an important validation of stellar physics and its wider application.

ACKNOWLEDGEMENTS

We thank R. Kurucz for allowing us to use the latest version of his codes and line lists in advance of publication. AD received support from the Australian Research Council under grant FL110100012. CC received support from NSF grant AST-1313280 and NASA grant NNX13AI46G.

REFERENCES

Anderson A. J., 1997, PhD thesis, Univ. California, Berkeley
Anderson J. et al., 2008, AJ, 135, 2055
Asplund M., Grevesse N., Sauval A. J., Scott P., 2009, ARA&A, 47, 481
Bedin L. R., Piotto G., Anderson J., Cassisi S., King I. R., Momany Y., Carraro G., 2004, ApJ, 605, L125
Cardelli J. A., Clayton G. C., Mathis J. S., 1989, ApJ, 345, 245
Carretta E., Gratton R. G., Lucatello S., Bragaglia A., Bonifacio P., 2005, A&A, 433, 597
Carretta E. et al., 2009a, A&A, 505, 117
Carretta E., Bragaglia A., Gratton R., Lucatello S., 2009b, A&A, 505, 139
di Criscienzo M., D'Antona F., Ventura P., 2010, A&A, 511, A70
Dotter A., Chaboyer B., Jevremović D., Baron E., Ferguson J. W., Sarajedini A., Anderson J., 2007a, AJ, 134, 376
Dotter A., Chaboyer B., Ferguson J. W., Lee H.-C., Worthey G., Jevremović D., Baron E., 2007b, ApJ, 666, 403
Dotter A., Chaboyer B., Jevremović D., Kostov V., Baron E., Ferguson J. W., 2008, ApJS, 178, 89
Ferguson J. W., Alexander D. R., Allard F., Barman T., Bodnarik J. G., Hauschildt P. H., Heffner-Wong A., Tamanai A., 2005, ApJ, 623, 585
Freeman K. C., Norris J., 1981, ARA&A, 19, 319
Girardi L., Castelli F., Bertelli G., Nasi E., 2007, A&A, 468, 657
Gratton R., Sneden C., Carretta E., 2004, ARA&A, 42, 385
Gratton R. G., Carretta E., Bragaglia A., 2012, A&AR, 20, 50
Grundahl F., Briley M., Nissen P. E., Feltzing S., 2002, A&A, 385, L14
Harris W. E., 1996, AJ, 112, 1487
Hauschildt P. H., Allard F., Baron E., 1999a, ApJ, 512, 377
Hauschildt P. H., Allard F., Ferguson J., Baron E., Alexander D. R., 1999b, ApJ, 525, 871
Iglesias C. A., Rogers F. J., 1996, ApJ, 464, 943
Kalirai J. S. et al., 2012, AJ, 143, 11
Kurucz R. L., 1970, SAO Special Report, 309
Kurucz R. L., 1993, SYNTHE Spectrum Synthesis Programs and Line Data (CD-ROM 18)
Kurucz R. L., Avrett E. H., 1981, SAO Special Report, 391
Lee Y.-W., Joo J.-M., Sohn Y.-J., Rey S.-C., Lee H.-C., Walker A. R., 1999, Nature, 402, 55
Marino A. F., Villanova S., Piotto G., Milone A. P., Momany Y., Bedin L. R., Medling A. M., 2008, A&A, 490, 625
Marino A. F., Villanova S., Milone A. P., Piotto G., Lind K., Geisler D., Stetson P. B., 2011, ApJ, 730, L16
Milone A. P. et al., 2008, ApJ, 673, 241
Milone A. P. et al., 2010, ApJ, 709, 1183
Milone A. P. et al., 2012, ApJ, 754, L34
Milone A. P. et al., 2013, ApJ, 767, 120
Milone A. P. et al., 2014, MNRAS, 439, 1588
Pietrinferni A., Cassisi S., Salaris M., Percival S., Ferguson J. W., 2009, ApJ, 697, 275
Piotto G., 2009, in Mamajek E. E., Soderblom D. R., Wyse R. F. G., eds, Proc. IAU Symp. 258, The Ages of Stars. Cambridge Univ. Press, Cambridge, p. 233
Prantzos N., Charbonnel C., Iliadis C., 2007, A&A, 470, 179
Richer H. B. et al., 2008, AJ, 135, 2141
Salaris M., Weiss A., Ferguson J. W., Fusilier D. J., 2006, ApJ, 645, 1131
Sarajedini A. et al., 2007, AJ, 133, 1658
Sbordone L., Bonifacio P., Castelli F., Kurucz R. L., 2004, Mem. Soc. Astron. Ital. Suppl., 5, 93
Sbordone L., Salaris M., Weiss A., Cassisi S., 2011, A&A, 534, A9
Schlafly E. F., Finkbeiner D. P., 2011, ApJ, 737, 103
Smith G. H., Briley M. M., 2005, PASP, 117, 895
Smith G. H., Briley M. M., 2006, PASP, 118, 740
Smith G. H., Briley M. M., Harbeck D., 2005, AJ, 129, 1589
VandenBerg D. A., Bergbusch P. A., Dotter A., Ferguson J. W., Michaud G., Richer J., Proffitt C. R., 2012, ApJ, 755, 15
Villanova S., Piotto G., Gratton R. G., 2009, A&A, 499, 755
Yong D., Grundahl F., Lambert D. L., Nissen P. E., Shetrone M. D., 2003, A&A, 402, 985
Yong D., Grundahl F., Nissen P. E., Jensen H. R., Lambert D. L., 2005, A&A, 438, 875
Yong D., Grundahl F., Johnson J. A., Asplund M., 2008, ApJ, 684, 1159
Yong D. et al., 2013, MNRAS, 434, 3542

APPENDIX A: ABUNDANCES FOR MODEL ATMOSPHERES AND OPACITIES

The abundances of the elements assumed in the models, determined from the abundance ratios listed in 1, for cases A and C are recorded here. The reference solar scale is that of Asplund et al. (2009). The log (A), number fractions, and mass fractions input to the stellar atmosphere codes, including low-temperature opacities, are given in Table A1. The number fractions for the 23 elements input to the OPAL web server are given in Table A2.

Table A1. Abundances used in model atmospheres, low-temperature opacities, and synthetic spectra.

	Population A			Population C		
El	log (*A*)	Num. frac.	Mass frac.	log (*A*)	Num. frac.	Mass frac.
H	12.00	9.215E−01	7.467E−01	12.00	9.215E−01	7.468E−01
He	10.93	7.843E−02	2.523E−01	10.93	7.843E−02	2.524E−01
Li	1.61	3.754E−11	2.095E−10	1.65	4.116E−11	2.297E−10
Be	− 0.27	4.948E−13	3.585E−12	− 0.23	5.426E−13	3.931E−12
B	1.05	1.033E−11	8.987E−11	1.09	1.133E−11	9.855E−11
C	6.53	3.122E−06	3.015E−05	6.12	1.214E−06	1.173E−05
N	6.07	1.082E−06	1.219E−05	7.57	3.423E−05	3.855E−04
O	7.69	4.513E−05	5.805E−04	7.11	1.187E−05	1.527E−04
F	2.91	7.490E−10	1.144E−08	2.95	8.212E−10	1.254E−08
Ne	6.68	4.410E−06	7.152E−05	6.72	4.836E−06	7.843E−05
Na	4.56	3.345E−08	6.184E−07	5.24	1.601E−07	2.960E−06
Mg	6.46	2.657E−06	5.194E−05	6.39	2.262E−06	4.421E−05
Al	5.08	1.107E−07	2.403E−06	5.98	8.800E−07	1.909E−05
Si	6.13	1.243E−06	2.806E−05	6.25	1.638E−06	3.700E−05
P	3.76	5.302E−09	1.320E−07	3.80	5.814E−09	1.447E−07
S	5.72	4.836E−07	1.246E−05	5.76	5.302E−07	1.367E−05
Cl	3.85	6.523E−09	1.859E−07	3.89	7.153E-09	2.039E−07
Ar	4.75	5.182E−08	1.664E−06	4.79	5.681E−08	1.824E−06
K	3.38	2.210E−09	6.949E−08	3.42	2.423E−09	7.619E−08
Ca	4.90	7.319E−08	2.358E−06	5.00	9.215E−08	2.969E−06
Sc	1.50	2.914E−11	1.053E−09	1.54	3.195E−11	1.154E−09
Ti	3.40	2.314E−09	8.910E−08	3.49	2.847E−09	1.096E−07
V	1.94	8.025E−11	3.287E−09	2.07	1.082E−10	4.434E−09
Cr	3.99	9.005E−09	3.764E−07	4.03	9.874E−09	4.128E−07
Mn	3.28	1.755E−09	7.755E−08	3.37	2.160E−09	9.541E−08
Fe	5.85	6.523E−07	2.929E−05	5.89	7.153E−07	3.211E−05
Co	3.31	1.881E−09	8.914E−08	3.32	1.925E−09	9.122E−08
Ni	4.51	2.981E−08	1.407E−06	4.58	3.503E−08	1.653E−06
Cu	1.88	6.990E−11	3.571E−09	1.98	8.800E−11	4.496E−09
Zn	2.91	7.490E−10	3.937E−08	2.95	8.212E−10	4.317E−08
Ga	1.39	2.262E−11	1.267E−09	1.43	2.480E−11	1.390E−09
Ge	2.00	9.215E−11	5.380E−09	2.04	1.010E−10	5.900E−09
As	0.65	4.116E−12	2.479E−10	0.69	4.513E−12	2.718E−10
Se	1.69	4.513E−11	2.866E−09	1.73	4.948E−11	3.142E−09
Br	0.89	7.153E−12	4.595E−10	0.93	7.843E−12	5.038E−10
Kr	1.60	3.668E−11	2.471E−09	1.64	4.022E−11	2.710E−09
Rb	0.87	6.831E−12	4.694E−10	0.91	7.490E−12	5.147E−10
Sr	1.22	1.529E−11	1.077E−09	1.26	1.676E−11	1.181E−09
Y	0.56	3.345E−12	2.391E−10	0.60	3.668E−12	2.622E−10
Zr	0.93	7.843E−12	5.752E−10	0.97	8.600E−12	6.307E−10
Nb	− 0.19	5.949E−13	4.444E−11	− 0.15	6.523E−13	4.873E−11
Mo	0.23	1.564E−12	1.206E−10	0.27	1.715E−12	1.322E−10
Ru	0.10	1.160E−12	9.426E−11	0.14	1.272E−12	1.033E−10
Rh	− 0.74	1.676E−13	1.387E−11	− 0.70	1.838E−13	1.521E−11
Pd	− 0.08	7.664E−13	6.558E−11	− 0.04	8.404E−13	7.191E−11
Ag	− 0.71	1.796E−13	1.558E−11	− 0.67	1.970E−13	1.708E−11
Cd	0.06	1.058E−12	9.563E−11	0.10	1.160E−12	1.048E−10
In	− 0.85	1.301E−13	1.201E−11	− 0.81	1.427E−13	1.317E−11
Sn	0.39	2.262E−12	2.159E−10	0.43	2.480E−12	2.367E−10
Sb	− 0.64	2.111E−13	2.066E−11	− 0.60	2.314E−13	2.266E−11
Te	0.53	3.122E−12	3.203E−10	0.57	3.423E−12	3.513E−10
I	− 0.10	7.319E−13	7.468E−11	− 0.06	8.026E−13	8.189E−11
Xe	0.59	3.585E−12	3.784E−10	0.63	3.930E−12	4.149E−10
Cs	− 0.57	2.480E−13	2.650E−11	− 0.53	2.719E−13	2.906E−11
Ba	0.53	3.122E−12	3.447E−10	0.57	3.423E−12	3.780E−10
La	− 0.55	2.597E−13	2.900E−11	− 0.51	2.847E−13	3.180E−11
Ce	− 0.07	7.843E−13	8.835E−11	− 0.03	8.600E−13	9.688E−11
Pr	− 0.93	1.082E−13	1.226E−11	− 0.89	1.187E−13	1.344E−11
Nd	− 0.23	5.426E−13	6.292E−11	− 0.19	5.949E−13	6.899E−11
Sm	− 0.69	1.881E−13	2.274E−11	− 0.65	2.063E−13	2.494E−11
Eu	− 1.13	6.831E−14	8.346E−12	− 1.09	7.490E−14	9.151E−12

Table A1. – *continued.*

El	log (*A*)	Population A Fraction By number	By mass	log (*A*)	Population C Fraction By number	By mass
Gd	– 0.58	2.423E−13	3.064E−11	– 0.54	2.657E−13	3.360E−11
Tb	– 1.35	4.116E−14	5.259E−12	– 1.31	4.513E−14	5.767E−12
Dy	– 0.55	2.597E−13	3.393E−11	– 0.51	2.847E−13	3.720E−11
Ho	– 1.17	6.230E−14	8.261E−12	– 1.13	6.831E−14	9.058E−12
Er	– 0.73	1.715E−13	2.307E−11	– 0.69	1.881E−13	2.530E−11
Tm	– 1.55	2.597E−14	3.527E−12	– 1.51	2.847E−14	3.867E−12
Yb	– 0.81	1.427E−13	1.985E−11	– 0.77	1.564E−13	2.177E−11
Lu	– 1.55	2.597E−14	3.653E−12	– 1.51	2.847E−14	4.006E−12
Hf	– 0.80	1.460E−13	2.095E−11	– 0.76	1.601E−13	2.298E−11
Ta	– 1.77	1.564E−14	2.276E−12	– 1.73	1.715E−14	2.496E−12
W	– 0.80	1.460E−13	2.158E−11	– 0.76	1.601E−13	2.367E−11
Re	– 1.39	3.754E−14	5.620E−12	– 1.35	4.116E−14	6.162E−12
Os	– 0.25	5.182E−13	7.925E−11	– 0.21	5.681E−13	8.690E−11
Ir	– 0.27	4.948E−13	7.647E−11	– 0.23	5.426E−13	8.385E−11
Pt	– 0.03	8.600E−13	1.348E−10	0.01	9.429E−13	1.479E−10
Au	– 0.73	1.715E−13	2.717E−11	– 0.69	1.881E−13	2.979E−11
Hg	– 0.48	3.051E−13	4.921E−11	– 0.44	3.345E−13	5.396E−11
Tl	– 0.75	1.638E−13	2.692E−11	– 0.71	1.796E−13	2.952E−11
Pb	0.10	1.160E−12	1.932E−10	0.14	1.272E−12	2.119E−10
Bi	– 1.00	9.215E−14	1.548E−11	– 0.96	1.010E−13	1.697E−11
Th	– 1.63	2.160E−14	4.029E−12	– 1.59	2.368E−14	4.418E−12
U	– 2.19	5.949E−15	1.138E−12	– 2.15	6.523E−15	1.248E−12

Table A2. Abundances used in the OPAL opacities.

EL	Population A Num. frac.	Population C Num. frac.
C	0.052 819	0.020 743
N	0.018 314	0.584 609
O	0.763 472	0.202 705
F	0.000 013	0.000 014
Ne	0.074 609	0.082 578
Na	0.000 566	0.002 734
Mg	0.044 957	0.038 625
Al	0.001 874	0.015 027
Si	0.021 028	0.027 981
P	0.000 090	0.000 099
S	0.008 181	0.009 055
Cl	0.000 110	0.000 122
Ar	0.000 877	0.000 970
K	0.000 037	0.000 041
Ca	0.001 238	0.001 573
Sc	0.000 000	0.000 001
Ti	0.000 039	0.000 049
V	0.000 001	0.000 002
Cr	0.000 152	0.000 169
Mn	0.000 030	0.000 037
Fe	0.011 036	0.012 214
Co	0.000 032	0.000 033
Ni	0.000 504	0.000 598

This paper has been typeset from a TEX/LATEX file prepared by the author.